White Rose Research Online

eprints@whiterose.ac.uk
https://eprints.whiterose.ac.uk
Universities of Leeds, Sheffield and York

Deposited via The University of York.

White Rose Research Online URL for this paper:
https://eprints.whiterose.ac.uk/id/eprint/244747/

Version: Published Version

Article:
Allison, Nicola, Castillo Alvarez, Cristina, Sinclair, Alice et al. (2026) Influences of saturation state, temperature, precipitation rate, Mg/Ca and amino acid inclusion on the aragonite Raman ν1 band: implications for interpreting marine calcifier biomineralisation. CrystEngComm. ISSN: 1466-8033

https://doi.org/10.1039/d6ce00413j

Reuse
This article is distributed under the terms of the Creative Commons Attribution (CC BY) licence. This licence allows you to distribute, remix, tweak, and build upon the work, even commercially, as long as you credit the authors for the original work. More information and the full terms of the licence here: https://creativecommons.org/licenses/

Takedown
If you consider content in White Rose Research Online to be in breach of UK law, please notify us by emailing eprints@whiterose.ac.uk including the URL of the record and the reason for the withdrawal request.

UNIVERSITY OF LEEDS
University of Sheffield
UNIVERSITY of York

CrystEngComm

ROYAL SOCIETY OF CHEMISTRY

PAPER

Published on 08 July 2026
Licensed under CC-BY 4.0

Check for updates

Cite this: *CrystEngComm*, 2026, **28**, 4759

Influences of saturation state, temperature, precipitation rate, Mg/Ca and amino acid inclusion on the aragonite Raman ν_1 band: implications for interpreting marine calcifier biomineralisation

Nicola Allison, *[ab] Cristina Castillo Alvarez,[ab] Alice Sinclair,[ab] Kirsty Penkman,[c] Sam Greeves,[c] Roland Kröger,[d] Matthieu Clog,[e] Catriona Nicholson,[a] Elynor Todd Jones,[a] Sophia Caton[a] and Adrian A. Finch[a]

The full width half maximum (FWHM) of the aragonite Raman ν_1 band is a potential proxy of the saturation state (Ω_{Ar}) of the media from which the aragonite precipitates, and is used to infer changes in the biomineralisation environment of marine calcifiers. However, controls on the FWHM are not fully understood. Here, we analyse the FWHM of a suite of aragonite samples synthesised *in vitro* under tightly controlled conditions. We vary temperature, Ω_{Ar} and pH independently during precipitation and determine how these parameters individually influence the FWHM. We also explore how the FWHM relates to aragonite precipitation rate, trace/minor element composition and biomolecule inclusion. The FWHM is positively related to Ω_{Ar}, aragonite growth rate and aragonite Mg/Ca. Although it is unclear which metric controls the FWHM, all likely increase structural disorder in the aragonite lattice. The incorporation of aspartic and glutamic acids in aragonite also significantly increases the FWHM, although it is unclear how inclusion of these amino acids in the proteins, which occur in biogenic aragonite, acts to alter FWHM. The sensitivity of the FWHM to Ω_{Ar} change is small (*i.e.* 0.0105 cm^{-1} for every 1 unit increase in Ω_{Ar}) suggesting that the FWHM has limited application in tracking the effects of ocean acidification on biogenic aragonite over decade to century time scales.

Received 20th May 2026,
Accepted 6th July 2026

DOI: 10.1039/d6ce00413j

rsc.li/crystengcomm

1. Introduction

Raman spectroscopy is a non-destructive analytical method that provides details on the structure and composition of materials. Raman scattering occurs when monochromatic light is scattered inelastically by interactions within a material. The energy difference between the incident and scattered photons (the Raman shift) corresponds to specific vibrations within the structure, providing a fingerprint to identify the material. Raman spectroscopy has been applied in the study of $CaCO_3$ materials to ascertain the polymorph,[1–3] to identify the presence of HCO_3^- in some biogenic carbonates[4] and to map the distribution of organic molecules in biogenic carbonates.[2]

The breadth (full width half maximum, FWHM) of the Raman ν_1 band at ~1085 cm^{-1} has been used as an indicator of the saturation state (Ω_{Ar}) from which aragonite forms[5] and to estimate Ω_{Ar} in the calcification media of tropical corals.[6] The ν_1 band represents symmetrical stretching of the C–O bond in the CO_3 group and the breadth of this peak increases with greater local disorder in the lattice around this group.[4] A perfectly crystalline $CaCO_3$ yields a narrow ν_1 band while a $CaCO_3$ containing physical defects and impurities (*i.e.* non-host ions) produces a wider ν_1 band, reflecting the broader distribution of C–O bond lengths in the material. Defects are more abundant in synthetic calcite formed at higher saturation states,[7] supporting the hypothesis that Ω influences the ν_1 band FWHM. However, previous studies indicate that the ν_1 band FWHM is also influenced by the inclusion of biomolecules in synthetic aragonite[8,9] and by the Mg content in synthetic high Mg calcite.[4] The aragonite ν_1 band FWHM may be positively related to the temperature in synthetic aragonite[10] but decreases in the aragonite skeletons of cultured corals at higher temperature,[10] indicating that controls on the ν_1 band FWHM are not fully understood.

[a] *School of Earth and Environmental Sciences, University of St. Andrews, KY16 9TS, UK. E-mail: na9@st-andrews.ac.uk*
[b] *Scottish Oceans Institute, University of St. Andrews, St Andrews, KY16 8LB, UK*
[c] *Department of Chemistry, University of York, York, UK*
[d] *Department of Physics, University of York, York, UK*
[e] *SUERC, University of Glasgow, UK*

In this study, we explore the effects of pH, Ω_{Ar}, temperature and biomolecules on the aragonite Raman spectrum ν_1 band FWHM. We analyse a series of synthetic aragonite samples precipitated *in vitro* from modified artificial seawater. These precipitations were conducted to determine how pH, temperature and Ω_{Ar} influence the precipitation rate and geochemistry of aragonite.[11–13] For the precipitations, we combined a pH stat titrator and a Ca^{2+} dosing system with an apparatus to control air stream [CO_2] to ensure that precipitating fluid pH, dissolved inorganic carbon (DIC), aqueous calcium (Ca^{2+}) and Ω_{Ar} remain essentially constant within each experiment.[11] We varied different parameters independently (*e.g.* pH, Ω_{Ar}, and temperature), to resolve their impact on the FWHM. We also analyse a series of aragonite samples precipitated in the presence and absence of key amino acids, which occur at high concentrations in biominerals, namely aspartic acid (Asp), glutamic acid (Glu) and glycine (Gly). We analyse the amino acid compositions of the precipitates to resolve the relationship between $[\text{amino acid}]_{\text{aragonite}}$ and the FWHM. Finally, Mg/Ca, Li/Ca and B/Ca have been reported previously for the same synthetic aragonite samples.[12,13] These minor/trace elements were measured to explore how the formation environment influences aragonite Li/Mg (a potential indicator of palaeotemperature[14] or aragonite growth rate[13]) and B/Ca (an indicator of seawater carbonate chemistry).[15] We utilise these data to determine how minor/trace element substitution relates to the FWHM. Our study provides a basis to interpret estimates of CO_3 group disorder in biogenic aragonite and to infer the biomineralisation environment.

2. Methods

2.1 Aragonite synthesis

Aragonite was precipitated *in vitro* from artificial seawater using a pH stat titrator (Metrohm Titrando 902) and the constant composition technique *i.e.* at constant pH, [DIC], Ω_{Ar} and [Ca].[11,16] Artificial seawater was prepared to the composition described by Millero (2013),[17] had a salinity of 35 and was stored in a 100 L container covered in thick gauge black plastic to exclude light. Prior to use, the seawater was filtered (0.2 μm polyether sulfone filter) and bubbled overnight with an atmospheric airstream (similarly filtered) in a water bath equipped with a chiller at the required treatment temperature. At the start of each experiment, 340 mL of the water was placed in a HDPE beaker (the reaction vessel) in the water bath and capped with an ethylene tetrafluoroethylene lid with ports through which a pH/temperature sensor (Metrohm Aquatrode PT1000), a propeller stirrer, a gas tube and 2 titrant dosing tubes were inserted. The DIC and pH of the seawater were adjusted to the required conditions by the addition of 0.6 M Na_2CO_3 (to increase DIC) and by 2 M HCl or NaOH (to control the pH). To provide a surface for precipitation, ~200 mg of an aragonite seed was added to the seawater (see below). $CaCO_3$ formation reduces the [CO_3^{2-}] of the precipitating solution and thereby reduces the pH. The pH sensor detects this decrease and the titrator automatically doses 0.45 M Na_2CO_3 to increase the solution pH to the initial value. The same volume of 0.45 M $CaCl_2$ + $SrCl_2$ in a 99 : 1 ratio is added to replace the Ca^{2+} and Sr^{2+} consumed during aragonite formation. This second titrant contains a mixture of Ca^{2+} and Sr^{2+} to replace the Sr^{2+} that substitutes for Ca^{2+} in the aragonite lattice.[18] The experiment finished after 6.7 mL of each titrant was added to the reaction vessel, indicating that 300 mg of aragonite was precipitated. The final solid was collected by filtration onto acid cleaned 0.2 μm polycarbonate filters (Nucleopore), rinsed with type 1 water and with trace element clean grade ethanol. Solids were dried at 40 °C and stored in a desiccator.

In the first set of experiments, aragonite samples were synthesised at 25 °C and over a range of pH and Ω_{Ar} values. The pH and Ω_{Ar} covary in experiments conducted in equilibrium with atmospheric CO_2.[11] To separate any influence of pH and Ω_{Ar} on aragonite structure, we conducted precipitations under different CO_2 atmospheres, *i.e.* varying [CO_3^{2-}] at constant pH and varying pH at similar [CO_3^{2-}]. Experimental conditions are summarised in Fig. 1a. Ω_{Ar} ranged from 4.0 to 17.8 and pH_{NBS} = 8.337, 8.545 or 8.727. To limit invasion or outgassing of CO_2 from the experimental solution, the gas tube into the vessel supplied air with the [CO_2] adjusted to be in equilibrium with the treatment seawater conditions. Ambient pCO_2 air streams used air sourced from outside the building and filtered and warmed before use. Above ambient CO_2 airstreams were produced by combining ambient air with high purity CO_2 using high precision mass flow controllers (SmartTrak 50 Series, Sierra USA). Below ambient CO_2 airstreams were produced by flowing ambient air through NaOH pellets to remove CO_2 and then combining this with high purity CO_2 as before. Airstream [CO_2] was determined using an infrared CO_2 analyser (WMA04, PP systems, USA). Similar experiments were conducted either with the addition of 2 mM of L-aspartic acid, L-glutamic acid or glycine. Amino acids were sourced from Sigma-Aldrich (purity ≥99%) and were dissolved in 1.5 mL of seawater and added to the titration vessel before the addition of Na_2CO_3.

In these experiments the seed was a ground coral skeleton with a surface area = 4.27 $m^2\ g^{-1}$ (Brunauer Emmett Teller, BET, technique).[19] In the second set of experiments, aragonite was synthesised at variable temperature (10 to 30 °C) and Ω_{Ar} (6.9 to 18.8). Experimental conditions are summarised in Fig. 1b. All experiments were conducted under conditions in equilibrium with atmospheric CO_2. In these experiments, the seed was a synthetic aragonite, produced at Ω_{Ar} = 11 and T = 25 °C and with a BET surface area of 7.00 $m^2\ g^{-1}$.[13]

Aragonite precipitation rates for each experiment were calculated by normalising the rate of titrant addition to the surface area of the seed. Solution [CO_3^{2-}] was calculated from measurements of [DIC] and pH at the start and end of each titration. The pH sensor was calibrated with fresh NIST

 This journal is © The Royal Society of Chemistry 2026

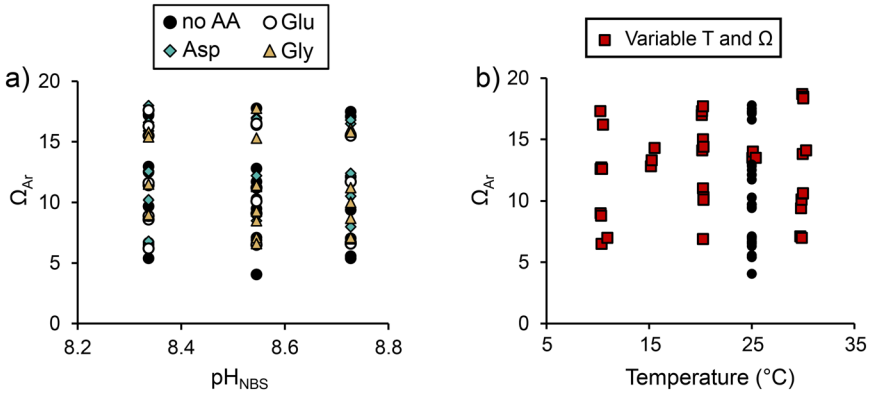

Fig. 1 Conditions used for aragonite synthesis in: (a) titrations conducted at 25 °C over variable pH and Ω_{Ar} in the presence and absence (no AA) of amino acids, and (b) titrations conducted at variable temperature and Ω_{Ar}. Experiments with no AA at 25 °C (from (a)) are shown by black dots in (b).

(National Institute of Standards and Technology) buffers each week and the pH is reported on the NBS scale.[20] The maximum drift in the pH sensor (estimated by measuring the pH in a fresh buffer, one week after calibration) was 0.004 pH units. Seawater [DIC] was measured at the end of each precipitation and at the start of a selection of precipitations[11,13] using a CO_2 differential, non-dispersive, infrared gas DIC analyser (Apollo SciTech; AS-C3) calibrated with a certified reference material (CRM 171 or 194, Scripps Institution of Oceanography). Three to eight replicate measurements of each sample were made using the DIC analyser giving a standard deviation of 0.22% on average and always <0.7%. Between the start and end of the titration, seawater DIC varied by <5% over the first set of precipitations[11] and by ~3%, on average, over the precipitations conducted at different temperatures.[13]

Solution [CO_3^{2-}] was estimated using CO2SYS, v2.1 (ref. 21) with the equilibrium constants for carbonic acid[22] and $KHSO_4$ (ref. 23) and using [B] seawater.[24] Solution Ω_{Ar} was calculated from [CO_3^{2-}] and measured [Ca^{2+}][11,13] coupled with the solubility product (K_{sp}) of aragonite at 1 atmosphere and the precipitation temperature.[25]

2.2 Raman spectroscopy

Raman spectra were collected with a Renishaw inVia Qontor Raman microscope, maintained in an air conditioned room at 20 °C. Spectra were collected in static mode from 100–1311 cm^{-1}, using a NIR 300 mW 785 nm solid state laser set at 5% full power, with a 1200 cm^{-1} grating and a spectral resolution of ~1 cm^{-1}. The laser spot was focused onto a particle of sample powder and data were collected for 2 s for each acquisition. Ten acquisitions were repeated on each spot and summed to yield the final spectrum. Collecting multiple spectra at the same location on a particle indicates that the ν_1 band FWHM is not influenced by repeated illumination by the laser under these conditions.[9] As the samples are powders, we consider the responses to be anisotropic. Twelve to fifteen spots were analysed on each sample powder. Background and ν_1 band counts in the final spectra are typically ~2000 and ~70 000, respectively. All the Raman spectra have lattice mode peaks at ~153 and 206 cm^{-1} (ref. 26) and a doublet ν_4 peak,[27] indicative of aragonite. Example spectra are shown in Fig. S1. The spectra were processed using OriginLabs peak processing software and the peak centre and the full width half maximum (FWHM) of the ν_1 band was estimated following a Voigt fit. The Voigt fit provides a better model of Raman vibration bands combined with instrumental artefacts than a Gaussian fit.[28] The measured FWHM is corrected to the true FWHM using the instrument spectral resolution,[29] which is ~1 cm^{-1}.

The spectrometer was calibrated using the 520 cm^{-1} vibrational model of a Si standard embedded within the instrument. To correct for drift in instrument performance within and between days, we analysed a milled synthetic aragonite powder[10] as an in-house reference material at intervals during each day of analyses. The reference material was analysed at up to 12 time points each day and at least 10 times at each time point. We reject any sample analyses if the reference material mean FWHM changes by >0.04 cm^{-1} between adjacent time points. We scale the FWHM of each sample to the mean FWHM of the bracketed reference material, assuming that the reference material has a FWHM = 4.32 cm^{-1}. Twenty-nine of the samples were analysed for more than 1 day. Duplicate samples run on different days agree within 0.026 cm^{-1} on average and always within <0.06 cm^{-1}.

2.3 Aragonite amino acid analysis

Aragonite amino acid compositions were analysed using the method of Hendy *et al.*, 2012 (ref. 30) (a modification of Kaufman and Manley, 1998 (ref. 31)). Less than 20 mg of aragonite was accurately weighed into a plastic microcentrifuge tube, bleached using 50 μL of 12% NaOCl per mg for 48 hours (to oxidise any amino acids not trapped within the crystal structure) and sequentially rinsed with 18.2 MΩ H_2O and methanol and dried

overnight. As the experimentally added amino acids were in the free form (not peptide-bound), samples were not hydrolysed before analysis but were demineralised in 2 M HCl (10 μL mg^{-1}) and spun to dryness in a centrifugal evaporator. Samples were rehydrated in a solution containing 0.01 mM L-homo-arginine (as an internal standard) and analysed using an Agilent 1100 reverse-phase HPLC with fluorescence detection. The final [amino acid] of the aragonite precipitated *in vitro* was calculated by correcting the [amino acid] of the final sample for the [amino acid] of the seed. Analyses of duplicate splits of the same synthetic samples indicates that the standard deviation (1σ) of repeat analyses is ~4%, 4% and 7% on average for Asp, Glu and Gly, respectively.

2.4 Scanning electron microscopy

We produced secondary electron scanning electron micrographs from selected precipitates using a JEOL 7800F Prime operated at a beam current of 0.04 nA and an accelerating voltage of 2 kV. Samples were not coated before viewing.

2.5 Data processing

We assume that Raman ν_1 band FWHM populations are normally distributed (as in ref. 10) and calculate the mean FWHM ± standard deviation (s) for each precipitate. We use multiple linear regression analysis to identify significant influences of different parameters on the FWHM. Precipitation rate and solution Ω_{Ar} covary in these experiments[11] while Mg/Ca

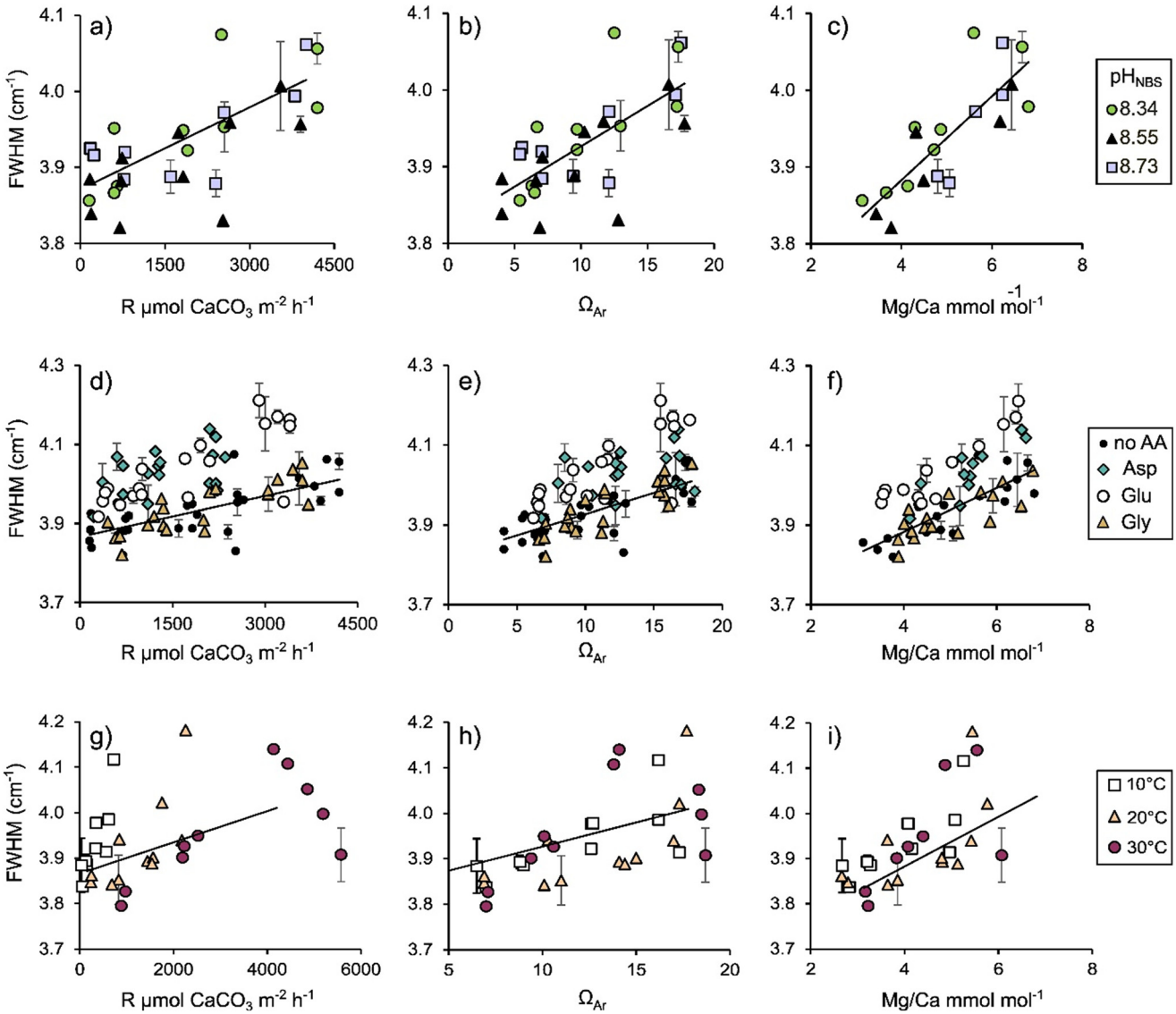

Fig. 2 Relationships between the Raman aragonite spectra ν_1 band FWHM and aragonite precipitation rate (R), seawater Ω_{Ar} and aragonite Mg/Ca for experiments: (a) to (c) at varying pH and Ω_{Ar} at 25 °C with no amino acids; (d) to (f) at varying pH and Ω_{Ar} at 25 °C with and without amino acids; and (g) to (i) at varying temperature and Ω_{Ar} without amino acids. Black lines indicate the linear best fit relationships for experiments conducted at 25 °C over varying pH and Ω_{Ar} with no amino acid. Error bars indicate the standard deviation of repeat analyses of the same sample on different days.

 This journal is © The Royal Society of Chemistry 2026

is strongly related to Ω_{Ar} and precipitation rate.[13] For this reason we undertake individual multiple linear regression analyses separately for each of these factors.

3. Results

3.1 Influences on the aragonite ν_1 FWHM

The SI summarises the mean Raman spectrum aragonite ν_1 band FWHM for all samples alongside experimental conditions (pH, [DIC] and Ω_{Ar}), aragonite precipitation rates and previously published data for aragonite B/Ca,[12] Li/Ca and Mg/Ca[13] (Tables S1 and S2). These minor/trace element data were measured by inductively coupled plasma mass spectrometry and were collected to determine how precipitating fluid conditions influence potential palaeoproxies.[12,13] We apply them here to explore relationships between minor/trace element incorporation and the aragonite ν_1 band FWHM.

We use multiple linear regression analysis to model the FWHM as a function of both solution pH and either Ω_{Ar}, precipitation rate or Mg/Ca in the experiments conducted without amino acids at 25 °C. As precipitation rate, Ω_{Ar} and aragonite Mg/Ca are related in these experiments, we undertake regression analyses separately for each of these factors. The FWHM is positively correlated with aragonite precipitation rate, seawater Ω_{Ar} and aragonite Mg/Ca (Fig. 2a–c respectively and Table 1) but is not significantly affected by aragonite Li/Ca or B/Ca (Fig. S2 and Table 1). The pH does not significantly affect the FWHM under any scenario (Table 1).

To determine how amino acids influence the FWHM, we use one way ANCOVA tests to compare linear relationships between the FWHM and aragonite precipitation rate, Ω_{Ar} or aragonite Mg/Ca, in the presence and absence of different amino acids. We combined all pH treatments for this as the previous analysis determined that the pH has no significant influence on the FHWM. The addition of aspartic acid or glutamic acid significantly increased the FWHM, after correcting for variance in aragonite precipitation rate, Ω_{Ar} or aragonite Mg/Ca while the addition of glycine had no significant effect on the FWHM (Fig. 2d–f and Table 2).

Table 2 ANCOVA p values comparing relationships between the FWHM and aragonite precipitation rate (R), Ω_{Ar} or Mg/Ca in the presence and absence of each of the tested amino acids (AA) at 25 °C. All pH treatments are combined for this analysis. ANCOVA tests for equal means (after correcting for variance) and equal slopes between populations. p values ≤ 0.05 are highlighted in bold

	p (equal means)	p (equal slopes)
R vs. FWHM		
2 mM Asp compared to no AA	$\mathbf{7.4 \times 10^{-10}}$	0.94
2 mM Gly compared to no AA	0.79	0.31
2 mM Glu acid compared to no AA	$\mathbf{7.6 \times 10^{-9}}$	**0.038**
Ω_{Ar} *vs.* FWHM		
2 mM Asp compared to no AA	$\mathbf{2.8 \times 10^{-5}}$	0.28
2 mM Gly compared to no AA	0.75	0.26
2 mM Glu compared to no AA	$\mathbf{2.8 \times 10^{-7}}$	0.053
Mg/Ca *vs.* FWHM		
2 mM Asp compared to no AA	$\mathbf{9.4 \times 10^{-5}}$	0.29
2 mM Gly compared to no AA	0.34	0.54
2 mM Glu compared to no AA	$\mathbf{1.3 \times 10^{-8}}$	0.10

In multiple linear regression analysis of the precipitations conducted over variable Ω_{Ar} and temperature, the FWHM is positively related with aragonite precipitation rate, seawater Ω_{Ar} and aragonite Mg/Ca (Fig. 2g–i and Table 1). Temperature does not significantly influence the FWHM in combination with Ω_{Ar} or aragonite Mg/Ca but has a significant effect in this dataset in combination with aragonite precipitation rate (Fig. 2g and Table 1). While the aragonite precipitation rate and FWHM are usually positively correlated, we note that at the 3 fastest aragonite precipitation rates (>4500 μmol $CaCO_3$ m^{-2} h^{-1}), the FWHM is relatively low (Fig. 2g).

3.2 Incorporation of amino acids in synthetic aragonite and FWHM

The $[\text{amino acid}]_{\text{aragonite}}$ of samples precipitated with amino acids under different conditions are summarised in Table S3 along with analyses of control samples (precipitated with no amino acids) and the seed used as a surface for aragonite growth. Minimal free Asp, Glu or Gly are detected in the

Table 1 Summary of p values and coefficients of determination generated in multiple linear regression (MLR) analysis modelling the ν_1 FWHM of aragonite precipitated without amino acids as a function of combinations of independent variables, *i.e.* of aragonite precipitation rate (R), Ω_{Ar}, $Mg/Ca_{aragonite}$, $Li/Ca_{aragonite}$ or $B/Ca_{aragonite}$ and of either pH or temperature (T). The figures associated with each test are indicated. p values ≤ 0.05 are highlighted in bold

Independent variables	MLR p values for each variable	r^2	Figure
Experiment set 1. Precipitations at 25 °C (n = 30) with no amino acid			
Precipitation rate and pH	$\mathbf{R = 2.1 \times 10^{-5}}$, pH = 0.66	0.50	Fig. 2a
Ω_{Ar} and pH	$\mathbf{\Omega_{Ar} = 1.8 \times 10^{-5}}$, pH = 0.57	0.50	Fig. 2b
Mg/Ca and pH	$\mathbf{Mg/Ca = 5.1 \times 10^{-6}}$, pH = 0.18	0.72	Fig. 2c
Li/Ca and pH	Li/Ca = 0.11, pH = 0.59	0.14	Fig. S2a
B/Ca and pH	B/Ca = 0.15, pH = 0.19	0.12	Fig. S2b
Experiment set 2. Precipitations at variable T (n = 34) with no amino acid			
Precipitation rate and T	$\mathbf{R = 2.5 \times 10^{-4}}$, $\mathbf{T = 6.0 \times 10^{-3}}$	0.36	Fig. 2g
Ω_{Ar} and T	$\mathbf{\Omega_{Ar} = 7.0 \times 10^{-5}}$, T = 0.95	0.41	Fig. 2h
Mg/Ca and T	$\mathbf{Mg/Ca = 1.0 \times 10^{-4}}$, T = 0.33	0.41	Fig. 2i

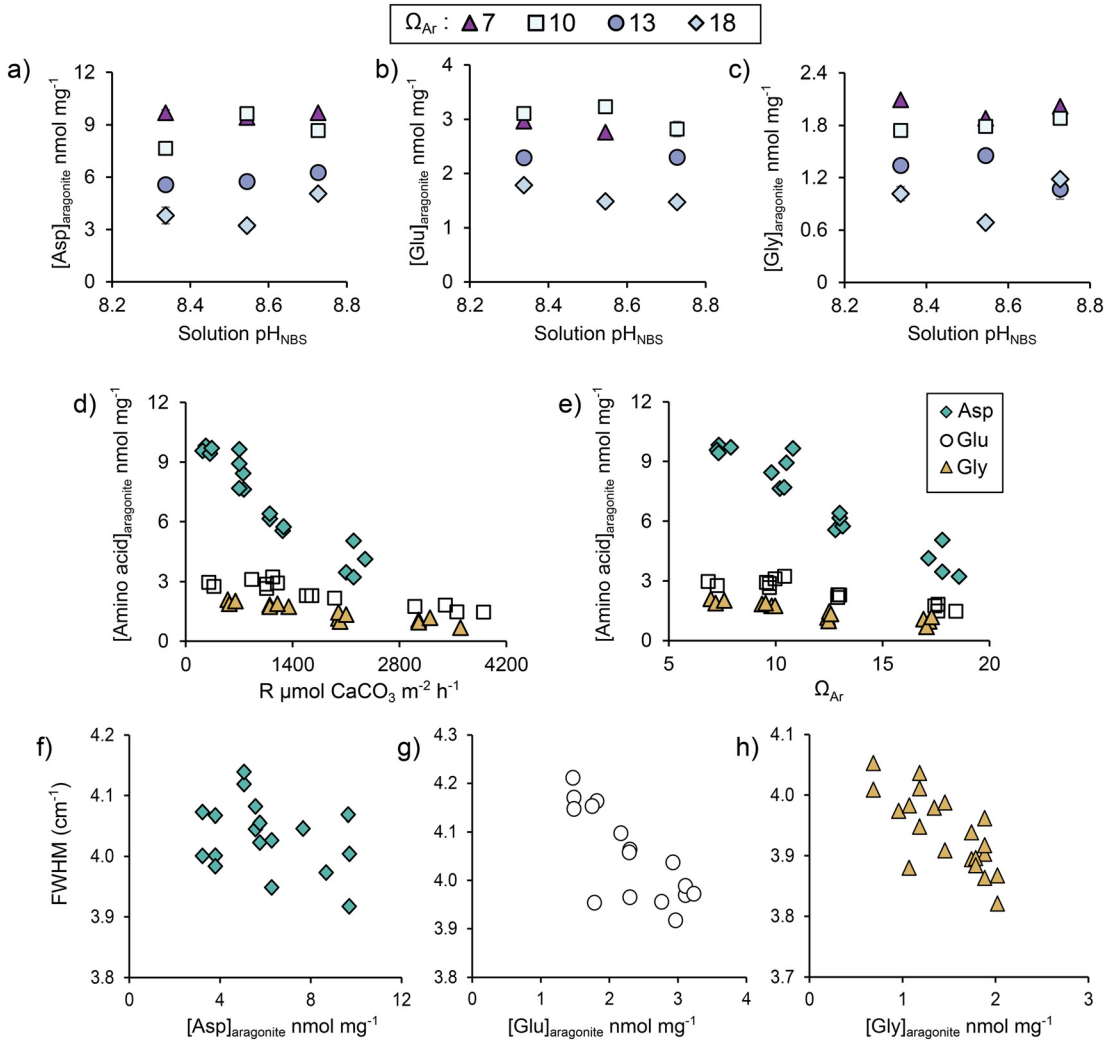

Fig. 3 Relationships between [amino acid]$_{aragonite}$ and various parameters. Influence of solution pH on aragonite: (a) Asp, (b) Glu and (c) Gly as a function of Ω_{Ar} at 25 °C. Relationships between [amino acid]$_{aragonite}$ and (d) precipitation rate (R), and (e) Ω_{Ar}. Relationships between the FWHM and [amino acid]$_{aragonite}$ for (f) Asp, (g) Glu and (h) Gly. Note: differences in y-axes (in a–c and f–h) and x-axes (in f–h) indicating differing incorporation of amino acids in aragonite.

control aragonite samples, precipitated with no amino acid. In the precipitations in the presence of 2 mM amino acids, Asp is incorporated at the highest concentrations in aragonite while Gly is incorporated at the lowest concentrations (Fig. 3a–c). In samples precipitated with amino acid, multiple linear regression analyses, modelling [amino acid]$_{aragonite}$ as a function of both solution pH and Ω, indicate that [amino acid]$_{aragonite}$ is significantly affected by solution Ω, but not by pH (Table 3 and Fig. 3a–c).

We observe significant linear inverse relationships between [amino acid]$_{aragonite}$ and both aragonite precipitation rate and solution Ω_{Ar} (Fig. 3d and e, Table 3). Halving the aragonite precipitation rate from the maximum rate observed increases [amino acid]$_{aragonite}$ by ~70% for Glu, by ~100% for Asp and by ~140% for Gly. Asp is incorporated at much higher concentrations in aragonite than Glu or Gly, especially at low precipitation rates (Fig. 3d), while Glu is incorporated at higher concentrations than Gly. We observe significant

Table 3 Summary of p values and coefficients of determination generated by regression analysis of relationships between [amino acid]$_{aragonite}$ and different parameters in experiments conducted with 2 mM [amino acid]$_{solution}$. p values ≤ 0.05 are highlighted in bold. Figures illustrating datasets are indicated

	Asp	Glu	Gly	Figure
[amino acid]$_{aragonite}$ *vs.* Ω_{Ar} and pH				
Ω_{Ar} p value	$\mathbf{6.1 \times 10^{-9}}$	**0.0076**	$\mathbf{4.8 \times 10^{-6}}$	Fig. 3a–c
pH p value	0.094	0.052	0.49	
r^2	0.95	0.56	0.84	
[amino acid]$_{aragonite}$ *vs.* precipitation rate				
p value	$\mathbf{1.1 \times 10^{-8}}$	**0.011**	$\mathbf{5.3 \times 10^{-7}}$	Fig. 3d
r^2	0.89	0.43	0.86	
[amino acid]$_{aragonite}$ *vs.* Ω_{Ar}				
p value	$\mathbf{7.3 \times 10^{-9}}$	**0.021**	$\mathbf{2.5 \times 10^{-6}}$	Fig. 3e
r^2	0.90	0.37	0.83	
ν_1 band FWHM *vs.* [amino acid]$_{aragonite}$				
p value	0.21	$\mathbf{3.8 \times 10^{-4}}$	$\mathbf{1.4 \times 10^{-4}}$	Fig. 3f–h
r^2	0.096	0.61	0.54	

This journal is © The Royal Society of Chemistry 2026

inverse relationships between the FWHM and both $[Glu]_{aragonite}$ and $[Gly]_{aragonite}$ but not with $[Asp]_{aragonite}$ (Fig. 3f–h and Table 3).

3.3 Aragonite morphology

Representative scanning electron micrographs of the surfaces of aragonite precipitated over a range of Ω_{Ar} and in the presence and absence of the amino acids are shown in Fig. 4. In all cases, the aragonite surface is composed of clusters of crystals where multiple crystals radiate from a common centre in each cluster. The radiating crystals have visible lengths of ~1 μm. At Ω_{Ar} = 18, the crystal surfaces appear roughened suggesting nanoporosity within the crystals.[12] At Ω_{Ar} = 7, the crystals have smoother surfaces suggesting they are infilled and less porous. At Ω_{Ar} = 18, the crystals usually taper to sharper tips that are pointier than those observed in the analogue samples precipitated at low Ω_{Ar}. Aragonite samples precipitated with aspartic acid are the exception to this, with sharp tips observed at the end of the crystals regardless of Ω_{Ar}.

Variations in crystal morphology are observed in aragonite samples precipitated at different temperature and Ω_{Ar} values (Fig. 5). The most rough/nanoporous crystals are precipitated at 30 °C with Ω_{Ar} = 13 or 18 or at 20 °C with Ω_{Ar} = 18. In contrast, the most solid/infilled crystals are produced at all temperatures and Ω_{Ar} = 7 or at 10 °C and Ω_{Ar} = 13.

4. Discussion

4.1 Controls on the aragonite Raman spectrum ν_1 band FWHM without amino acids

The Raman ν_1 band FWHM in aragonite precipitated with no amino acid is significantly positively related to precipitating fluid Ω_{Ar}, aragonite precipitation rate and aragonite Mg/Ca (Fig. 2a–c). Positive correlations between Ω_{Ar} and the FWHM in synthetic aragonite samples have been reported previously.[5,10] In addition, the FWHM in tropical and deep water coral skeletons is positively correlated with skeletal Mg/Ca.[32] The broadening of the ν_1 band encodes variations in the transition energy values associated with the vibrational mode, which could have several causes. This may reflect a drop in symmetry of the CO_3 group such that it is no longer an equilateral triangle (*i.e.* departing from the D_{3h} point symmetry), which might follow, for example, protonation to create a HCO_3 group. Other forms of

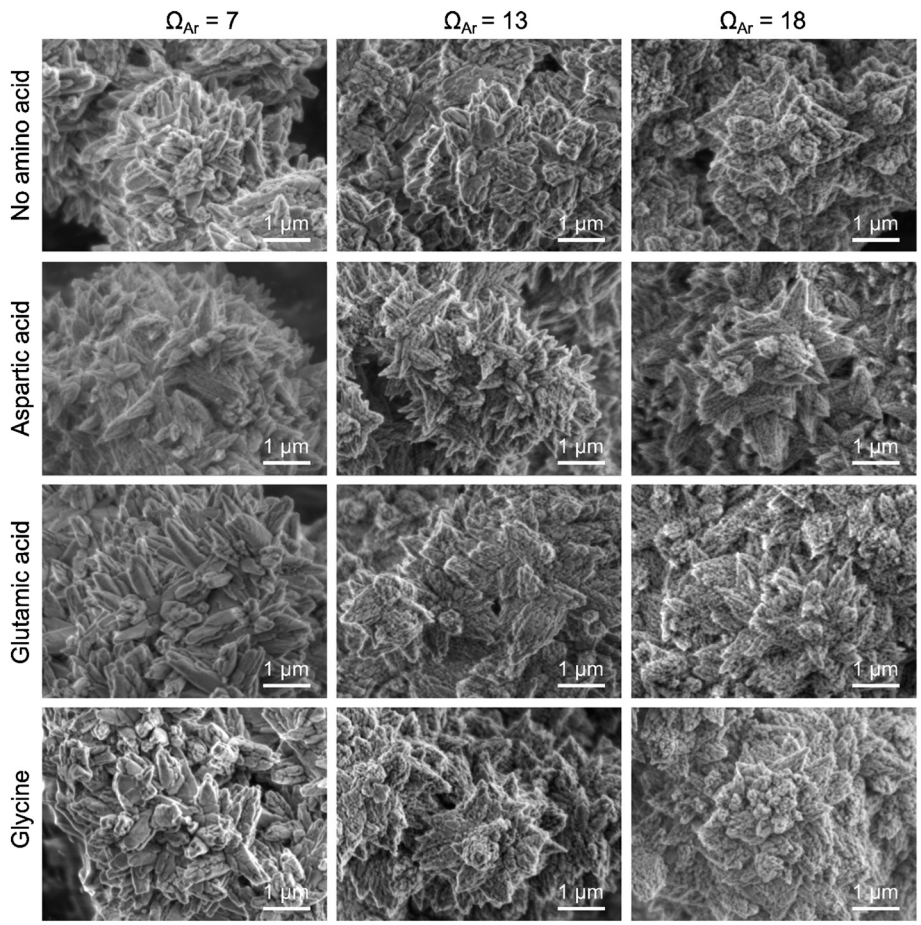

Fig. 4 Scanning electron micrographs of aragonite precipitates formed over varying seawater Ω_{Ar} (at pH_{NBS} = 8.73) and in the presence and absence of amino acids (2 mM).

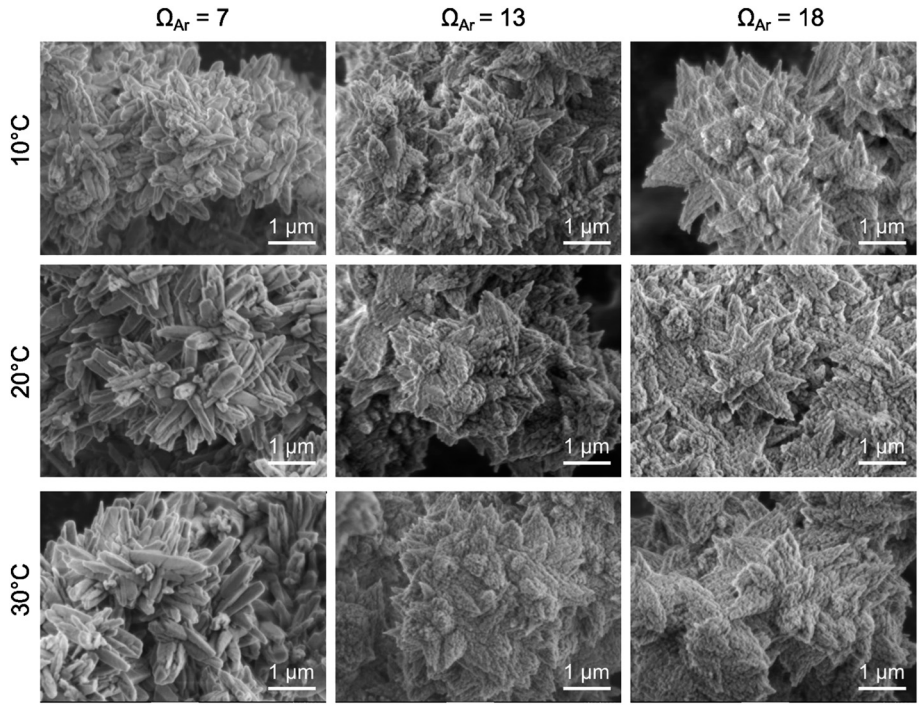

Fig. 5 Scanning electron micrographs of aragonite precipitates formed over varying temperature and seawater Ω_{Ar}.

disorder do not relate to a local drop in point symmetry but rather to the wider environment in which the carbonate group is found. In aragonite, planar CO_3 groups are arranged in layers, perpendicular to the *c*-axis. The CO_3 groups in alternate layers are orientated in opposite directions.[32] Structural disorder, local to the CO_3 group, occurs when CO_3 groups are disturbed from their idealised locations. This may occur if, 1) the CO_3 group sits adjacent to a substituent ion replacing Ca, which changes the "stiffness" of the structure around the carbonate group. Substitution of Ca by smaller ions will increase the FWHM whereas substitution by larger ions will narrow it. Alternatively, 2) disruption of the regular structure of the CO_3 group layers can occur if the alternating layers have a stacking defect, such that one plane is in the same orientation as the layer below. If a structure has many such stacking defects, it can be considered as a mosaic of phase domains and anti-phase domains (nanotwins) of aragonite. 3) The carbonate group may tilt such that it is no longer perpendicular to the *c*-axis. This might follow substitution of segments of the structure, such as the replacement of entire CO_3 groups with organic molecules or the generation of vacancies around the carbonate group. Finally, 4) substitution of trace elements may create local environments, which equate to other carbonate structural types, as observed during Mn incorporation into mollusc shells.[33]

Rapid $CaCO_3$ precipitation rates are associated with an increase in lattice defects,[7] providing an explanation for the positive relationship between the FWHM and both Ω_{Ar} and precipitation rate. In addition, the aragonite samples analysed here were precipitated from an artificial seawater and we incorporate a range of trace and minor elements. Trace/minor elements may substitute for the host ions Ca^{2+} and CO_3^{2-} in the aragonite lattice[18,34,35] or may be hosted interstitially between crystal lattice sites.[36] The incorporation of non-host ions in $CaCO_3$ can create lattice distortions. For example, bond distances in aragonite are 2.53, 2.58 and 2.07 Å respectively for Ca–O, Sr–O and Mg–O,[37] and Mg incorporation shortens the *a*- and *c*-axis lengths of the unit cell in synthetic aragonites.[38] In the present study, the ν_1 vibration widens with increased Mg incorporation. Similarly, increasing the Mg content of high magnesium calcite broadens the Raman ν_1 band FWHM.[4] Sr and Mg contents of cnidarians and molluscs are also inferred to influence the infrared aragonite ν_2 band wavelength, another indicator of the CO_3 group vibration,[39] providing more evidence of the role of minor/trace elements in lattice disorder. The FWHM is not influenced by Li or B in the present study (Table 1). This is likely due to the higher concentration of Mg/Ca in the aragonite (2.7 to 6.8 mmol mol^{-1}) compared to B/Ca (0.36 to 0.63 mmol mol^{-1}) or Li/Ca (3.8 to 7.8 μmol mol^{-1}).

It is predicted that Ω_{Ar}, precipitation rate and Mg/Ca are positively related to the FWHM. Ω_{Ar} and $CaCO_3$ precipitation rates are positively related[11,40] and the incorporation of Mg in aragonite is also positively related to aragonite precipitation rate.[13,41,42] The incorporation of trace and minor elements in $CaCO_3$ is controlled by the relative rates at which these non-host ions attach and detach from the growing crystal face and diffuse through the mineral–fluid boundary compared to the behaviour of the host ions.[43,44] This explains the similarities observed in the influence of aragonite growth rate and Mg/Ca on the FWHM. We also observe that Ω_{Ar} and temperature influence aragonite habit

 This journal is © The Royal Society of Chemistry 2026

and surface roughness (Fig. 4 and 5). Pointier crystals are generated at higher temperatures or Ω_{Ar} and indicate that crystal growth is favoured on particular faces under these conditions. Mg^{2+} adsorption can inhibit growth on specific crystal faces in calcite, thereby influencing crystal morphology.[45] Our observation of variations in aragonite morphology between samples provides a mechanism to explain the observed relationship between Mg incorporation in aragonite and the FWHM.

Although the FWHM is positively correlated with aragonite precipitation rate and Ω_{Ar}, this relationship breaks down in experiments with high Ω_{Ar} (>18) and temperature (30 °C). In these experiments, the FWHM is relatively narrow (Fig. 2g). $CaCO_3$ precipitation can occur *via* heterogeneous nucleation (*i.e.* by growth on an existing surface), or *via* homogeneous nucleation (*i.e.* by creation of a crystal). Homogeneous $CaCO_3$ nucleation is not observed in seawater at 25 °C at $\Omega_{calcite}$ ≤18, equivalent to Ω_{Ar} ≈12.[46,47] Homogeneous nucleation is more likely to occur at higher Ω_{Ar} and higher temperatures.[47] We hypothesise that homogeneous nucleation occurs in our experiments at high Ω_{Ar} and temperature, and that aragonite formed *via* this route exhibits a narrower FWHM than aragonite formed *via* heterogeneous nucleation.

Water temperature significantly influences the FWHM *versus* precipitation rate relationship (Fig. 2g and Table 1), with lower temperatures associated with a broader FWHM than their high temperature counterparts produced at similar precipitation rates. The incorporation of Mg in aragonite is positively related to aragonite precipitation rate[13,41,42] but inversely related to temperature.[13,42] Fig. 2g exhibits a broad similarity in the distribution of points compared to a plot of $D_{Mg/Ca}$ (the distribution coefficient of Mg in aragonite, effectively an indicator of aragonite [Mg]) as a function of precipitation rate and temperature (Fig. 2d in Castillo Alvarez *et al.*, 2025 (ref. 13)). This suggests that aragonite Mg/Ca is a better indicator of the FWHM than precipitation rate.

We observe no influence of aragonite B/Ca on the FWHM, although an inverse relationship has been reported between B/Ca and the FWHM in aragonitic tropical and deep sea corals.[32] Boron speciation is pH dependent[48] and $B(OH)_4^-$, the aqueous species favoured at higher pH seawater, is incorporated into the aragonite lattice.[34,35,49] For this reason B/Ca in synthetic aragonite is principally controlled by pH under the conditions inferred to occur in coral calcification media.[12] Aragonite B/Ca is not significantly influenced by Ω_{Ar} or aragonite precipitation rate under these conditions.[12] B/Ca in coral aragonite is likely controlled by the pH of the coral calcification media, and, at present, it is unclear how this varied over the tropical and deep sea coral dataset.[32]

4.2 Influence of amino acids on the FWHM

The Raman ν_1 band FWHM significantly increases in aragonite precipitated in the presence of 2 mM Asp and Glu when the FWHM is plotted as function of precipitation rate and Ω_{Ar} (Fig. 2d and e and Table 1). 2 mM Gly has no significant effect on the FWHM (Fig. 2d and e and Table 1). This agrees with previous studies, which report that aspartic acid can increase the FWHM[8,9] while glycine has no significant influence.[9] Aragonite Mg/Ca is significantly increased in aragonite precipitated in the presence of Asp (but not Glu or Gly) as a function of aragonite precipitation rate.[13] However, the FWHM significantly increases in aragonite precipitated with Asp or Glu when the FWHM is plotted as function of aragonite Mg/Ca (Fig. 2f and Table 1), indicating that the amino acids do not increase the FWHM solely by enhancing the incorporation of Mg into the aragonite lattice.

Analysis of the aragonite samples precipitated in the presence of the amino acids indicates that all three biomolecules are incorporated into the aragonite. Aspartic acid adsorbs onto the surface of calcite[50] and adsorbed amino acids can become entrapped in the mineral by subsequent $CaCO_3$ growth. The incorporation of Asp and Gly increases the *a*- and *c*- dimensions in synthetic calcite[51,52] and the incorporation of biomolecules in biogenic carbonates is hypothesised to explain the lattice distortions in these materials compared to non-biogenic geological analogues.[32,53,54] We conclude that Asp and Glu incorporation enhances CO_3 group local disorder in aragonite. Gly has no significant influence on the FWHM but we note that Gly is smaller and incorporated at lower concentrations in aragonite compared to the other two amino acids (Fig. 3). It also does not have a functional group on the side chain, likely reducing its ability to adsorb onto the aragonite face.

Amino acid incorporation is inversely related to solution Ω_{Ar} for all amino acids (Fig. 3e). It is unclear why amino acid incorporation increases at low Ω_{Ar} and precipitation rate, but the observation implies that amino acid adsorption to aragonite is enhanced at lower aragonite growth rates. Aragonite precipitated with aspartic acid exhibits a pointy crystal morphology (Fig. 4), suggesting that adsorption of this amino acid to specific crystal faces controls aragonite habit. Aspartic acid may also alter calcite crystal morphology by adsorbing preferentially onto particular faces.[55] In addition, trace element attachment/detachment rates in $CaCO_3$ are influenced by the presence of non-host ions on the crystal surface[44,56] and the reduced aragonite Mg/Ca observed in precipitates formed at low Ω_{Ar} (Fig. 2f) may also influence amino acid adsorption/desorption.

The relationship between $[amino\ acid]_{aragonite}$ and the FWHM is not straightforward. Amino acids are incorporated at the highest concentrations in synthetic experiments, which are conducted at low Ω_{Ar} and which produce the slowest aragonite precipitation rates but we observe an inverse correlation between $[Glu]_{aragonite}$ (and $[Gly]_{aragonite}$) and the FWHM (Fig. 3g and h and Table 3). This is because the FWHM is reduced at low Ω_{Ar}.

4.3 Applications of the aragonite FWHM

Our analysis indicates that the aragonite Raman spectrum ν_1 band FWHM is positively related to Ω_{Ar}, aragonite growth rate

and aragonite Mg/Ca. As Ω_{Ar}, aragonite precipitation rate and aragonite Mg/Ca covary, and it is unclear which actual metric controls the FWHM. We observe an average increase in an FWHM of 0.0105 cm^{-1} for every increase in Ω_{Ar} of 1, indicating that the sensitivity of the FWHM to the Ω_{Ar} change is relatively small in the present study. DeCarlo *et al.* (2017)[5] observed a greater influence of Ω_{Ar} on the FWHM but did not replace the seawater Ca^{2+} consumed in aragonite synthesis during their precipitations. The drop of [Ca^{2+}] during their experiments likely influences aragonite precipitation rate and seawater Mg/Ca (and thereby incorporation of Mg in aragonite). Both factors likely also influence the FWHM.

To put the sensitivity of the FWHM to Ω_{Ar} in context, we note that seawater Ω_{Ar} in the tropical Pacific Ocean warm pool decreased by 0.0083 $year^{-1}$ between 1985 and 2016.[57] The global tropical surface seawater pH is predicted to decrease by ~0.3 pH units between 1850–1990 and 2081–2100 under climate model scenario RCP8.5,[58] equivalent to a change in seawater Ω_{Ar} of ~0.009 $year^{-1}$. These 2 estimates of present/ongoing seawater Ω_{Ar} decrease are in good agreement. It is not clear how coral calcification Ω_{Ar} responds to changes in seawater Ω_{Ar}. Corals can increase the pH of the calcification media more under ocean acidification scenarios[59] and may be able to increase Ca^{2+} transport to the calcification site.[60] Both mechanisms increase calcification media Ω_{Ar} suggesting that ocean acidification driven changes in calcification media Ω_{Ar} are smaller than those observed in ambient seawater.

Repeat Raman analyses of the same synthetic sample in the present study yield a typical standard deviation of 0.06 cm^{-1} and we estimate that approximately 40 analyses on the same sample are required to generate a 95% confidence limit on the FWHM of ±0.02 cm^{-1}, equivalent to an error in Ω_{Ar} of ±2. This is a large error in comparison with observed changes in seawater Ω_{Ar} over decadal and century time scales.[57,58] In addition, we observe considerable noise in the dataset describing the relationship between the FWHM and Ω_{Ar} combined with temperature (r^2 = 0.41, Table 1) indicating that these metrics account for less than half of the FWHM variance observed in the dataset. This suggests that the FWHM is an insensitive indicator of precipitating media Ω_{Ar}.

We also note that the FWHM is increased when aragonite is precipitated in the presence of 2 mM Asp or Glu (Fig. 2d–f). Relating the significance of these observations to biogenic minerals is complicated. In this study, we observe aragonite [Asp] and [Glu] of 3 to 10 nmol mg^{-1} and 1.5 to 3.0 nmol mg^{-1} respectively in the synthetic precipitates. These concentrations are generally higher than those observed in biogenic aragonite samples. Asp and Glu in biogenic minerals are measured as Asx (aspartic acid and asparagine) and Glx (glutamic acid and glutamine), respectively. Asparagine and glutamine undergo deamination during the hydrolysis preparation step of amino acid analysis, so they cannot be differentiated from Asp and Glu. The ratios of Asp to asparagine and of Glu to glutamine are both approximately 10 : 1 in coral acidic amino acid rich skeletal protein CARP 3,[61] suggesting that estimates of Asx and Glx in biogenic minerals predominantly reflect Asp and Glu. [Asx] and [Glx] range from 0.3 to 1.3 nmol mg^{-1} and 0.1 to 0.4 nmol mg^{-1} respectively in coral skeletons,[10,62,63] and from 0.3 to 1.2 nmol mg^{-1} and 0.3 to 0.6 nmol mg^{-1} respectively in mollusc shells.[64]

At Ω_{Ar} ~12 (the estimated Ω_{Ar} of coral calcification fluid,[65] [Asp] and [Glu] are ~6 nmol mg^{-1} and 2.2 nmol mg^{-1} respectively in synthetic aragonite precipitated from 2 mM amino acid solutions, *i.e.* about 5× the concentrations observed in coral aragonite. The relationship between $[amino\ acid]_{solution}$ and $[amino\ acid]_{aragonite}$ is approximately linear,[9] suggesting that the [Asp] and [Glu] of the calcification media is ~0.4 mM for each amino acid. At Ω_{Ar} ~12, the FWHM of the synthetic aragonite is increased by ~0.1 cm^{-1} by 2 mM of both amino acids and assuming a linear relationship between $[amino\ acid]_{aragonite}$ and the FWHM we can calculate that the inclusion of Asp and Glu at the typical concentrations that occur in coral skeletons increases the FWHM by ~0.02 cm^{-1}. In biominerals, amino acids are predominantly incorporated in aragonite as peptides and proteins rather than as free amino acids.[64] Preliminary results suggest that Asp and tetra-aspartic acid have broadly comparable effects on the FWHM for each Asp residue incorporated,[9] but further work is required to predict the effect of incorporation of larger peptides and proteins in aragonite. We recognise that skeletal amino acid concentrations vary significantly in response to seawater pCO_2[62] and temperature[10] and even between individuals of the same species.[10] Further work is required to clarify if this influences the FWHM based estimates of coral calcification fluid Ω_{Ar}.

Conclusions

This study demonstrates that the aragonite Raman spectrum ν_1 band FWHM is positively influenced by Ω_{Ar}, aragonite growth rate and aragonite Mg/Ca. There are several physical processes that influence the FWHM of the Raman bands. Structural disorder occurs when CO_3 groups are displaced from their idealised locations, which is more likely at fast aragonite precipitation rates (associated with high Ω_{Ar}) and when more Mg is incorporated into the lattice. Incorporation of aspartic and glutamic acids into aragonite also increases the FWHM. We infer that the sensitivity of the FWHM to the Ω_{Ar} change is too small and other factors are too dominant for it to be an effective indicator of the Ω_{Ar} of coral calcification media.

Author contributions

Conceptualisation: NA, AF, KP, RK and MC. Investigation: CCA, NA, AS, KP, SG, RK, CN, ETJ and SC conducted the study. Funding acquisition: NA, AF, KP, RK and MC. Data curation, formal analysis, and visualization: NA. Writing – original draft: NA. Writing – review & editing: All.

 This journal is © The Royal Society of Chemistry 2026

Conflicts of interest

There are no conflicts to declare.

Data availability

The supplementary information (SI) contains all data.

Supplementary information: Fig. S1. Example Raman spectra of synthetic aragonite precipitated in the presence and absence of 2 mM aspartic acid. Fig. S2. Relationships between the Raman aragonite spectrum ν_1 band FWHM and (a) $Li/Ca_{aragonite}$ and (b) $B/Ca_{aragonite}$. Table S1. Details of precipitation conditions, aragonite [amino acid], n1 band FWHM and Mg/Ca, Li/C and B/Ca (where known) in precipitations conducted at 25 °C. Table S2. Details of precipitation conditions, ν_1 band FWHM and Mg/Ca, Li/C and B/Ca (where known) in precipitations conducted over variable temperature and Ω. Table S3. Aragonite precipitation conditions and $[amino\ acid]_{aragonite}$ in seeds and precipitated aragonite. See DOI: https://doi.org/10.1039/d6ce00413j.

Acknowledgements

This work was supported by the UK Natural Environment Research Council (NE/S001417/1 to NA, KP, RK, MC and AAF). Participation of CN, SC and ETJ in this study was supported by the University of St Andrews STARIS scheme. We thank David Miller and Aaron Naden, University of St Andrews, for assistance with Raman analyses. The use of the Raman microscope at the University of St. Andrews is supported by the EPSRC Light Element Analysis Facility Grant EP/T019298/1 and the EPSRC Strategic Equipment Resource Grant EP/R023751/1.

References

1 L. Addadi, S. Raz and S. Weiner, *Adv. Mater.*, 2003, **15**, 959–970, DOI: 10.1002/adma.200300381.
2 G. Nehrke and J. Nouet, *Biogeosciences*, 2011, **8**, 3761–3769, DOI: 10.5194/bg-8-3761-2011.
3 B. Purgstaller, V. Mavromatis, A. Immenhauser and M. Dietzel, *Geochim. Cosmochim. Acta*, 2016, **174**, 180–195, DOI: 10.1016/j.gca.2015.10.030.
4 W. D. Bischoff, S. K. Sharma and F. T. MacKenzie FT, *Am. Mineral.*, 1985, **70**, 581–589.
5 T. M. DeCarlo, J. P. D'Olivo, T. Foster, M. Holcomb, T. Becker and M. T. McCulloch, *Biogeosciences*, 2017, **14**, 5253–5269.
6 J. C. Hankins and T. M. DeCarlo, *Sci. Adv.*, 2025, **11**, eadr0264.
7 F. Suzana, S. S. Lee, I. Calvo-Almazán, W. Cha, R. Harder and P. Fenter, *Adv. Mater.*, 2024, **36**, 2310672.
8 C. Kellock, M. C. Castillo Alvarez, A. A. Finch, K. Penkman, R. Kröger, M. Clog and N. Allison, *PLoS One*, 2022, **17**, e0278627.
9 G. Gardella, M. C. Castillo Alvarez, S. Presslee, A. A. Finch, K. Penkman, R. Kröger, M. Clog and N. Allison, *Cryst. Growth Des.*, 2024, **24**, 9379–9390.
10 N. Allison, P. Ross, C. Castillo Alvarez, K. Penkman, R. Kröger, C. Kellock, C. Cole, M. Clog, D. Evans, C. Hintz and K. Hintz, *Coral Reefs*, 2024, **43**, 1317–1329.
11 M. C. Castillo Alvarez, K. Penkman, R. Kröger, A. A. Finch, M. Clog, A. Brasier, J. Still and N. Allison, *Geochim. Cosmochim. Acta*, 2024, **364**, 184–194.
12 M. C. Castillo Alvarez, K. Penkman, R. Kröger, A. A. Finch, M. Clog, E. Hathorne and N. Allison, *Geochim. Cosmochim. Acta*, 2024, **379**, 39–52.
13 M. C. Castillo Alvarez, E. Hathorne, M. Clog, A. A. Finch, R. Kröger, K. Penkman and N. Allison, *Commun. Earth Environ.*, 2025, **6**, 984.
14 P. Montagna, M. McCulloch, E. Douville, M. L. Correa, J. Trotter, R. Rodolfo-Metalpa, D. Dissard, C. Ferrier-Pages, N. Frank, A. Freiwald and S. Goldstein, *Geochim. Cosmochim. Acta*, 2014, **132**, 288–310.
15 K. A. Allen and B. Hönisch, *Earth Planet. Sci. Lett.*, 2012, **345**, 203–211.
16 R. Beck, M. Seiersten and J. P. Andreassen, *J. Cryst. Growth*, 2013, **380**, 187–196.
17 F. J. Millero, *Chemical Oceanography*, CRC Press, Boca Raton, 3rd edn, 2013.
18 A. A. Finch, N. Allison, S. R. Sutton and M. Newville, *Geochim. Cosmochim. Acta*, 2003, **67**, 1197–1202.
19 S. Brunauer, P. H. Emmett and E. Teller, *J. Am. Chem. Soc.*, 1938, **60**, 309–319.
20 A. G. Dickson, *Geochim. Cosmochim. Acta*, 1984, **48**, 2299–2308.
21 D. Pierrot, E. D. Lewis and W. R. Wallace, *MS Excel Program Developed for CO_2 System Calculations*, Oak Ridge National Laboratory, 2006.
22 T. J. Lueker, A. G. Dickson and C. D. Keeling, *Mar. Chem.*, 2000, **70**, 105–119.
23 A. G. Dickson, *Chem. Thermodyn.*, 1990, **22**, 113–127.
24 K. Lee, T. W. Kim, R. H. Byrne, F. J. Millero, R. A. Feely and Y. M. Liu, *Geochim. Cosmochim. Acta*, 2010, **74**, 1801–1811.
25 A. Mucci, *Am. J. Sci.*, 1983, **283**, 780–799.
26 T. M. DeCarlo, *Nat. Commun.*, 2018, **9**, 5325.
27 J. Urmos, S. K. Sharma and F. T. Mackenzie, *Am. Mineral.*, 1991, **76**, 641–646.
28 R. J. Meier, *Vib. Spectrosc.*, 2005, **39**, 266–269.
29 L. Nasdala, A. Banerjee, T. Hager and W. Hofmeister, *Microscopy and Analysis*, 2001, pp. 11–14.
30 E. J. Hendy, P. J. Tomiak, M. J. Collins, J. Hellstrom, A. W. Tudhope, J. M. Lough and K. E. Penkman, *Geochim. Cosmochim. Acta*, 2012, **86**, 338–353.
31 D. S. Kaufman and W. F. Manley, *Quat. Sci. Rev.*, 1998, **17**, 987–1000.
32 G. A. Farfan, A. Apprill, A. Cohen, T. M. DeCarlo, J. E. Post, R. G. Waller and C. M. Hansel, *Coral Reefs*, 2022, **41**, 19–34.
33 A. L. Soldati, D. E. Jacob, P. Glatzel, J. C. Swarbrick and J. Geck, *Sci. Rep.*, 2016, **6**, 22514.
34 S. Sen, J. Stebbins, N. Hemming and B. Ghosh, Coordination environments of B impurities in calcite and aragonite polymorphs: a ^{11}B MAS NMR study, *Am. Mineral.*, 1994, **79**, 819–825.

35 K. Klochko, G. D. Cody, J. A. Tossell, P. Dera and A. J. Kaufman, *Geochim. Cosmochim. Acta*, 2009, **73**, 1890–1900.

36 A. Zhadan, V. Montouillout, J. Aufort, V. Mavromatis and E. Balan, High-resolution solid-state 7Li NMR study of lithium incorporation in calcite and aragonite, *Chem. Geol.*, 2025, 122842.

37 A. A. Finch and N. Allison, *Mineral. Mag.*, 2007, **71**, 539–552.

38 M. Boon, W. D. Rickard, A. L. Rohl and F. Jones, *Cryst. Growth Des.*, 2020, **20**, 5006–5017.

39 Y. Dauphin, *Appl. Spectrosc.*, 1997, **51**, 253–258.

40 E. A. Burton and L. M. Walter, *Geology*, 1987, **15**, 111–114.

41 R. I. Gabitov, A. K. Schmitt, M. Rosner, K. D. McKeegan, G. A. Gaetani, A. L. Cohen, E. B. Watson and T. M. Harrison, *Geochem., Geophys., Geosyst.*, 2013, **12**, Q03001.

42 V. Mavromatis, J. M. Brazier and K. E. Goetschl, *Geochim. Cosmochim. Acta*, 2022, **317**, 53–64.

43 O. Branson, Boron incorporation into marine $CaCO_3$, in *Boron Isotopes: The Fifth Element*, ed. H. Marschall and G. Foster, Springer International Publishing, 2018, pp. 71–105.

44 D. J. DePaolo, *Geochim. Cosmochim. Acta*, 2011, **75**, 1039–1056.

45 F. C. Meldrum and S. T. Hyde, *J. Cryst. Growth*, 2001, **231**, 544–558.

46 J. W. Morse, D. K. Gledhill and F. J. Millero, *Geochim. Cosmochim. Acta*, 2003, **67**, 2819–2826.

47 J. W. Morse and S. He, *Mar. Chem.*, 1993, **41**, 291–297.

48 A. G. Dickson, *Deep-Sea Res.*, 1990, **37**, 755–766.

49 J. Noireaux, V. Mavromatis, J. Gaillardet, J. Schott, V. Montouillout, P. Louvat, C. Rollion-Bard and D. Neuville, *Earth Planet. Sci. Lett.*, 2015, **430**, 398–407.

50 R. M. Hazen, T. R. Filley and G. A. Goodfriend, *Proc. Natl. Acad. Sci. U. S. A.*, 2001, **98**, 5487–5490, DOI: 10.1073/pnas.101085998.

51 S. Borukhin, L. Bloch, T. Radlauer, A. H. Hill, A. N. Fitch and B. Pokroy, *Adv. Funct. Mater.*, 2012, **22**, 4216–4224.

52 Y. Y. Kim, J. D. Carloni, B. Demarchi, D. Sparks, D. G. Reid, M. E. Kunitake, C. C. Tang, M. J. Duer, C. L. Freeman, B. Pokroy, K. Penkman, J. H. Harding, L. A. Estroff, S. P. Baker and F. C. Meldrum, *Nat. Mater.*, 2016, **15**, 903–910.

53 B. Pokroy, J. P. Quintana, E. A. N. Caspi, A. Berner and E. Zolotoyabko, *Nat. Mater.*, 2004, **3**, 900–902.

54 B. Pokroy, A. N. Fitch, F. Marin, M. Kapon, N. Adir and E. Zolotoyabko, *J. Struct. Biol.*, 2006, **155**, 96–103.

55 H. Nada, *J. Phys. Chem. C*, 2014, **118**, 14335–14345.

56 M. J. Henehan, C. D. Klein Gebbinck, J. V. B. Wyman, M. P. Hain, J. W. B. Rae, B. Hönisch, G. L. Foster and S. T. Kim, *Geochim. Cosmochim. Acta*, 2022, **318**, 510–530.

57 M. Ishii, K. B. Rodgers, H. Y. Inoue, K. Toyama, D. Sasano, N. Kosugi, H. Ono, K. Enyo, T. Nakano, D. Iudicone and B. Blanke, *Global Biogeochem. Cycles*, 2020, **34**, e2019GB006368.

58 H. O. Pörtner, D. C. Roberts, V. Masson-Delmotte, P. Zhai, M. Tignor, E. Poloczanska and N. M. Weyer, *IPCC special report on the ocean and cryosphere in a changing climate*, 2019, vol. 1155, pp. 10–17.

59 A. A. Venn, E. Tambutté, N. Caminiti-Segonds, N. Techer, D. Allemand and S. Tambutté, *Sci. Rep.*, 2019, **9**, 1–12.

60 D. A. Armstrong and K. D. Bahr, *ICES J. Mar. Sci.*, 2025, **82**, fsaf050.

61 T. Mass, J. L. Drake, L. Haramaty, J. D. Kim, E. Zelzion, D. Bhattacharya and P. G. Falkowski, *Curr. Biol.*, 2013, **23**, 1126–1131.

62 C. Kellock, C. Cole, K. Penkman, D. Evans, R. Kröger, C. Hintz, K. Hintz, A. A. Finch and N. Allison, *Sci. Rep.*, 2020, **10**, 12797.

63 A. Sinclair, S. Fitzer, S. Greeves, K. Penkman, C. Sangmanee and N. Allison, *Coral Reefs*, 2025, **44**, 1617–1629.

64 K. E. H. Penkman, D. S. Kaufman, D. Maddy and M. J. Collins, *Quat. Geochronol.*, 2008, **3**, 2–25.

65 D. S. Sevilgen, A. A. Venn, M. Y. Hu, E. Tambutté, D. de Beer, V. Planas-Bielsa and S. Tambutté, *Sci. Adv.*, 2019, **5**, eaau7447.

 This journal is © The Royal Society of Chemistry 2026